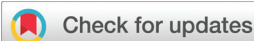


## RESEARCH ARTICLE

[View Article Online](#)  
[View Journal](#)


Cite this: DOI: 10.1039/d5qi01143d

# Enhancing edge chemistry in HCP-Ru catalysts through crystalline domain engineering for efficient alkaline hydrogen evolution†

 Shuai Zhao,<sup>a</sup> Jie Xu,<sup>b</sup> Chang Wang,<sup>a</sup> Hailang Zhang,<sup>a</sup> Qiangchun Liu<sup>\*a</sup> and Xiangkai Kong<sup>\*a,c</sup>

Engineering the nanoscale domain structure of transition metal catalysts offers a promising pathway to enhance their intrinsic activity by tailoring surface coordination and electronic states. Here, we report a MgO-assisted solvothermal strategy for synthesizing hexagonal close-packed (HCP) Ru nanospheres from Ru(acac)<sub>3</sub> in isopropanol, in which MgO templates modulate the crystallization pathway to preferentially expose the (100) and (002) facets while suppressing the (101) facet. This facet-selective growth leads to the formation of well-defined crystalline domains with abundant low-coordination edge sites and oxygen vacancies at domain boundaries. Such domain-induced surface reconstruction gives rise to edge-rich chemistry – a catalytic environment characterized by enhanced interfacial charge transfer, strengthened water adsorption, and optimized hydrogen binding at under-coordinated Ru<sup>0</sup> sites. Mechanistic studies, including *in situ* Raman spectroscopy, reveal that the edge-enriched Ru<sub>domains</sub> promotes earlier onset of hydrogen adsorption and accelerates H<sub>2</sub> evolution by facilitating both the Volmer and Heyrovsky steps. Benefiting from these structural and electronic advantages, the resulting Ru<sub>domains</sub> achieves an ultralow overpotential of 23.5 mV at 10 mA cm<sup>-2</sup> and a small Tafel slope of 34.4 mV dec<sup>-1</sup> in alkaline media, outperforming commercial Pt/C and most Ru-based HER catalysts. This work highlights a general and scalable strategy for activating edge sites through oxide-directed facet/domain engineering, providing new insight into the design of HER electrocatalysts based on edge-rich chemistry.

Received 14th May 2025,

Accepted 11th July 2025

DOI: 10.1039/d5qi01143d

[rsc.li/frontiers-inorganic](https://rsc.li/frontiers-inorganic)

## 1. Introduction

The intensifying energy crisis and environmental concerns from fossil fuel combustion have significantly disrupted the sustainable development of human society.<sup>1–3</sup> Clean energy and renewable energy can fundamentally solve the problem of ecological deterioration.<sup>4–6</sup> Hydrogen production *via* the electrochemical splitting of water is regarded as a viable method for sustainable energy retention and long-term power sustainability.<sup>7,8</sup> Within alkaline aqueous electrolytes, platinum-based materials and their alloy systems are universally recognized as the standard for cata-

lytic efficacy in the hydrogen evolution reaction, but these benchmark catalysts have some shortcomings, such as low abundance, poor performance, elevated costs and poor durability over time, hindering their wide adoption.<sup>9,10</sup> Recent decades have witnessed significant progress in developing high-efficiency catalytic materials with enhanced specific activity.<sup>11,12</sup> Compared with Pt/C, Ru has a relatively low cost and similar hydrophilicity to Pt, which makes it a promising material for HER electrocatalysts.<sup>13,14</sup> In alkaline electrolytes, due to the shortage of hydrogen ions, hydrogen ions need to be first dissociated from water molecules near the catalyst surface under the influence of the reaction potential, and then H<sup>+</sup> adsorption–desorption occurs at the active site.<sup>15</sup> This pathway involves an initial step of water dissociation, referred to as the Volmer step, followed by the hydrogen combination process, either through the Tafel or the Heyrovsky step. The reaction kinetics are largely determined by how effectively water dissociates and hydrogen binding.<sup>16,17</sup> Furthermore, ruthenium has a high hydrolytic dissociation capacity, which is conducive to increasing the efficiency of the Volmer step. The firm metal–H bond at the ruthenium site is beneficial for hydrogen adsorption. Due to their remarkable properties and stability,

<sup>a</sup>Anhui Province Key Laboratory of Pollutant Sensitive Materials and Environmental Remediation, Huaibei Normal University, Huaibei, Anhui, 235000, P. R. China.

E-mail: [qchliu@chnu.edu.cn](mailto:qchliu@chnu.edu.cn)

<sup>b</sup>School of Chemistry and Chemical Engineering, Nanjing University, Nanjing, Jiangsu, 210023, P. R. China

<sup>c</sup>School of Materials and Physics, China University of Mining and Technology, Xuzhou, Jiangsu, 221116, P. R. China. E-mail: [xkong@cumt.edu.cn](mailto:xkong@cumt.edu.cn)

† Electronic supplementary information (ESI) available. See DOI: <https://doi.org/10.1039/d5qi01143d>

ruthenium materials, encompassing both monatomic and oxide forms, have captured significant scientific attention in the realm of hydrogen evolution.<sup>18–20</sup>

Crystal plane engineering can accurately control the surface atomic arrangement and electronic structure by exposing highly active crystal planes, leading to a reduction in the reaction energy barrier and an increase in mass-specific activity.<sup>21,22</sup> In recent years, researchers have devoted themselves to developing and controlling the crystal plane orientation and grain boundary density of materials to boost their catalytic properties. For instance, Kang *et al.* proposed that exposing only the (111) crystal plane in high entropy alloy octahedral nanocrystals enables pH-universal high-efficiency electrocatalytic hydrogen evolution.<sup>23</sup> At the same time, grain boundaries, a key type of crystal defect, can induce the redistribution of local electrons and form highly active sites. By constructing a Ru/Ru<sub>x</sub>Fe<sub>3-x</sub>O<sub>4</sub> heterointerface, Mu *et al.* found that lattice mismatch led to the formation of abundant defect sites and twisted interface structures significantly boosted HER activity.<sup>24</sup> Despite these advances, conventional strategies for defect and facet control are often complex, costly, and difficult to scale. Notably, the catalytic role of localized edge chemistry arising from small crystalline domains, referred to here as “edge-rich chemistry,” remains underexplored. Domain structures, consisting of nanoscale crystalline subunits with abundant grain boundaries, can synergistically introduce surface defects.<sup>25–27</sup> These features collectively lower the activation energy for water dissociation and enhance H\* binding dynamics, offering a promising route for intrinsic HER acceleration.<sup>28,29</sup>

Here, we greatly improve the catalytic performance of metallic ruthenium by using a MgO-induced solvothermal strategy to synthesize domain-rich HCP-Ru nanocrystals with preferential facet orientation. Due to the limiting effect of magnesium oxide on the growth of ruthenium, the size of agglomerated spherical ruthenium metal decreases. Meanwhile, a large number of crystal domains are formed around the ruthenium nanosphere, resulting in more active areas, and a strong polarization effect occurs between the interfaces, which greatly promotes the improvement of catalytic activity while maintaining stability. Structural characterization methods including XRD and HRTEM confirm the formation of enhanced (100)/(002) planes and reduced (101) contributions. Furthermore, XPS, EPR, and FTIR analyses confirm the generation of oxygen vacancies and under-coordinated Ru–O species-defect motifs known to facilitate the Volmer step by accelerating water activation and promoting H\* intermediate stabilization. Electrochemical testing reveals that the sample synthesized with an optimal MgO content exhibits the best HER performance in alkaline media, correlating with the synergistic effects of domain-induced edge-rich chemistry, optimized facet exposure, and defect-driven Volmer step facilitation. This study provides new insights into domain and facet engineering in noble metal catalysts and demonstrates the effectiveness of oxide-induced directional growth for boosting electrocatalytic activity.

## 2. Experimental

### 2.1 Preparation of pristine Ru and Ru<sub>domains</sub>

50 mg Ru(acac)<sub>3</sub> and a certain amount of MgO were dissolved in a solution containing 30 mL of isopropanol and DI water. After continuous magnetic stirring at room temperature for 30 minutes, the solution, which was homogeneous, was transferred to a 50 mL Teflon-lined stainless steel reactor and a solvothermal reaction was carried out at 180 °C for 12 h. Following the gradual cooling of the reaction system to room temperature, the sediment was taken out of the solution, and then 10 mL of 8 M HNO<sub>3</sub> was added and left to stand for a few minutes until the white bottom disappeared. Next, the product was washed several times with deionized water and absolute ethanol and then treated with freeze drying. Finally, a series of products were obtained. Based on the dosage of MgO (0, 20, 60, and 180 mg), the products were named pristine Ru, Ru<sub>domains</sub>-1, Ru<sub>domains</sub>, and Ru<sub>domains</sub>-2.

### 2.2 Preparation of D-Ru<sub>domains</sub>

The preparation procedure was the same as that for Ru<sub>domains</sub>, except that 8 M nitric acid was replaced with 1 M nitric acid.

### 2.3 Preparation of N–MgO

The preparation procedure was the same as that for Ru<sub>domains</sub>, except that Ru(acac)<sub>3</sub> was not added and no acid washing was performed.

Details on materials, physicochemical characterization, and electrochemical measurement are available in the ESI.†

## 3. Results and discussion

The preparation process is shown in Fig. 1a. Ru was incorporated into MgO by a solvothermal method, and the obtained intermediate was Ru/MgO/Mg(OH)<sub>2</sub>. MgO, recognized as an alkaline oxide, was later purified with NO<sub>3</sub><sup>-</sup> to obtain the final Ru<sub>domains</sub> products.<sup>30,31</sup> The introduced template is a sacrificial template; due to the limiting effect of magnesium oxide on the growth of Ru, the size of agglomerated spherical ruthenium metal decreases. After being pickled with nitric acid, a large number of crystal domains are formed around the Ru nanosphere, facilitating the exposure of abundant edge sites, thereby enhancing catalytic activity.<sup>32</sup>

The morphologies of the samples were characterized by SEM. As demonstrated in Fig. 1b and c and Fig. S1,† pristine Ru shows smooth spheres (150–210 nm), whereas Ru<sub>domains</sub> exhibits roughened surfaces and reduced size (110–170 nm). The same phenomenon occurs in the samples of Ru<sub>domains</sub>-1 and Ru<sub>domains</sub>-2 (Fig. S2†), attributed to MgO regulation. Pristine Ru shows negligible morphological changes before acid treatment (Fig. S3a†). However, for the unwashed Ru<sub>domains</sub> (Fig. S3b†), a mixture of spherical Ru particles and flake-like structures is observed, with both components tightly integrated. XRD patterns (Fig. 2c) confirm that the flake-like structures consist of MgO and Mg(OH)<sub>2</sub>. Notably, small projections also formed around unpickled Ru<sub>domains</sub>, indicating that

the surface protrusions are not due to etching but originate from initial structural limitations. Elemental mapping demonstrated the spherical morphology of pristine Ru and Ru<sub>domains</sub> (Fig. S4†) and the uniform spread of Ru throughout the whole substrate. To further verify how MgO/Mg(OH)<sub>2</sub> is distributed in the sample, we prepared the D-Ru<sub>domains</sub> sample. As shown in Fig. 1d, elemental mapping of D-Ru<sub>domains</sub> reveals uniform dispersion of both Ru and Mg within the spherical architecture, thus conclusively supporting that Mg species are intimately associated with Ru prior to their complete removal. This spatial coupling effectively influenced Ru nanostructure development and, upon template removal, yielded a surface enriched with exposed edges and active centers. TEM further illustrated structural evolution. Fig. S5a† shows a TEM image of pristine Ru, consisting of compact spherical particles without distinct edge features. Ru<sub>domains</sub> (Fig. S5d†) displayed prominent nanoscale protrusions and sheet-like branches (Fig. S5d1 and d2†), indicating a higher surface area and edge enrichment. With increasing MgO content, the morphology evolved toward irregularity accompanied by a decrease in average Ru particle size (Fig. S5b, c, and S6†), thereby confirming the dual role of MgO in growth suppression and nanostructural refinement. Furthermore, as clearly observed in Fig. S7† (a high-resolution image of D-Ru<sub>domains</sub>), the outer part of the Ru nanospheres is coated with MgO.

pieces, and a lattice distance of 0.202 nm corresponds to the (101) plane of Ru crystals (Fig. 2c), indicating a hexagonal close-packed structure (HCP). Fig. 2b shows the HRTEM image of Ru<sub>domains</sub>; lattice directions are arranged differently and through measurement, the interfacial spacing of the crystal planes is found to be 0.202 nm, 0.215 nm, and 0.233 nm, corresponding to the (101), (002), and (100) planes of Ru, respectively (Fig. 2b1 and b2). Furthermore, abundant crystalline domains were formed on the outer surface of Ru<sub>domains</sub> within the nanospheres, which are composed of lattice fringes in different small regions (Fig. 2b). Similar phenomena can be observed in samples Ru<sub>domains</sub>-1 and Ru<sub>domains</sub>-2 (Fig. S8 and S9†). Additionally, the presence of crystal domains was obviously observed on the outer surface of Ru nanospheres of D-Ru<sub>domains</sub> (Fig. S10†). The findings suggest that MgO not only limits the overgrowth of Ru nanocrystals but also forms a strong interaction with the Ru surface during synthesis. Following the removal of MgO *via* nitric acid etching, the long-range lattice ordering of Ru was disrupted, thereby leading to the formation of abundant crystalline domains coupled with surface defect engineering (Fig. S11†).<sup>33</sup> Induced defects enable more sites to become active and visible on the Ru nanosphere surface, maximizing atom usage and accelerating the catalytic process.<sup>34</sup> The creation of localized lattice disorder

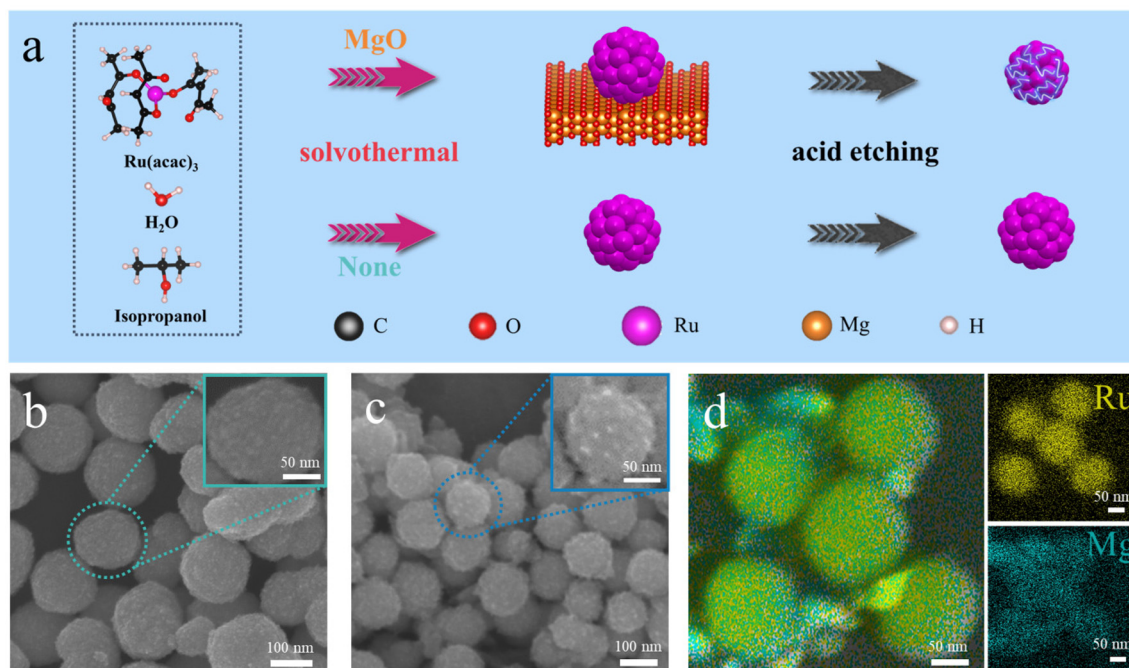


**Fig. 1** (a) Schematic illustration of the preparation of pristine Ru and Ru<sub>domains</sub>. (b and c) SEM images of pristine Ru and Ru<sub>domains</sub>, with different magnifications shown in the insets. (d) SEM image and elemental mapping of D-Ru<sub>domains</sub>.

High-resolution transmission electron microscopy (HRTEM) offered additional confirmation of the crystal structure of the sample. As illustrated in Fig. 2a, we can clearly see that lattice directions are uniformly arranged on the small

and different crystal faces at domain boundaries underpins what we define as “edge-rich chemistry”. The X-ray diffraction (XRD) patterns of the various samples are displayed (Fig. 2c and S12†). Each sample exhibited six characteristic peaks at

38.4°, 42.2°, 44°, 58.3°, 69.4°, and 78.4° corresponding to hexagonal close-packed (HCP) Ru (PDF#89-3942) with no magnesium signals observed, confirming complete template removal. Compared with pristine Ru, Ru<sub>domains</sub> exhibited a decreased (101) diffraction intensity and enhanced (002)/(100) peaks, in line with HRTEM observations. This suggests the formation of multi-domain structures and loss of long-range crystalline order.<sup>35</sup> Furthermore, the (101) peak of Ru<sub>domains</sub> exhibited a shift toward lower angles (Fig. S13a†), implying lattice expansion caused by strong Ru–MgO interfacial strain.<sup>36</sup>

pristine Ru, the Ru<sub>domains</sub> on Ru–Ru appears very faint, indicating weak vibrations due to their low crystallinity, in good agreement with the XRD results. For pristine Ru and Ru<sub>domains</sub>, three peaks at 503.8, 623.8, and 690.8 cm<sup>-1</sup> are observed, corresponding to the E<sub>g</sub>, A<sub>1g</sub>, and B<sub>2g</sub> vibrational modes of the Ru–O bond, respectively.<sup>38</sup> Increasing the MgO content progressively weakens the B<sub>2g</sub> vibrational modes of Ru–O bonds, indicating surface oxidation and structural disruption.<sup>39</sup> These spectral changes support the presence of crystalline domains and high-density defects.

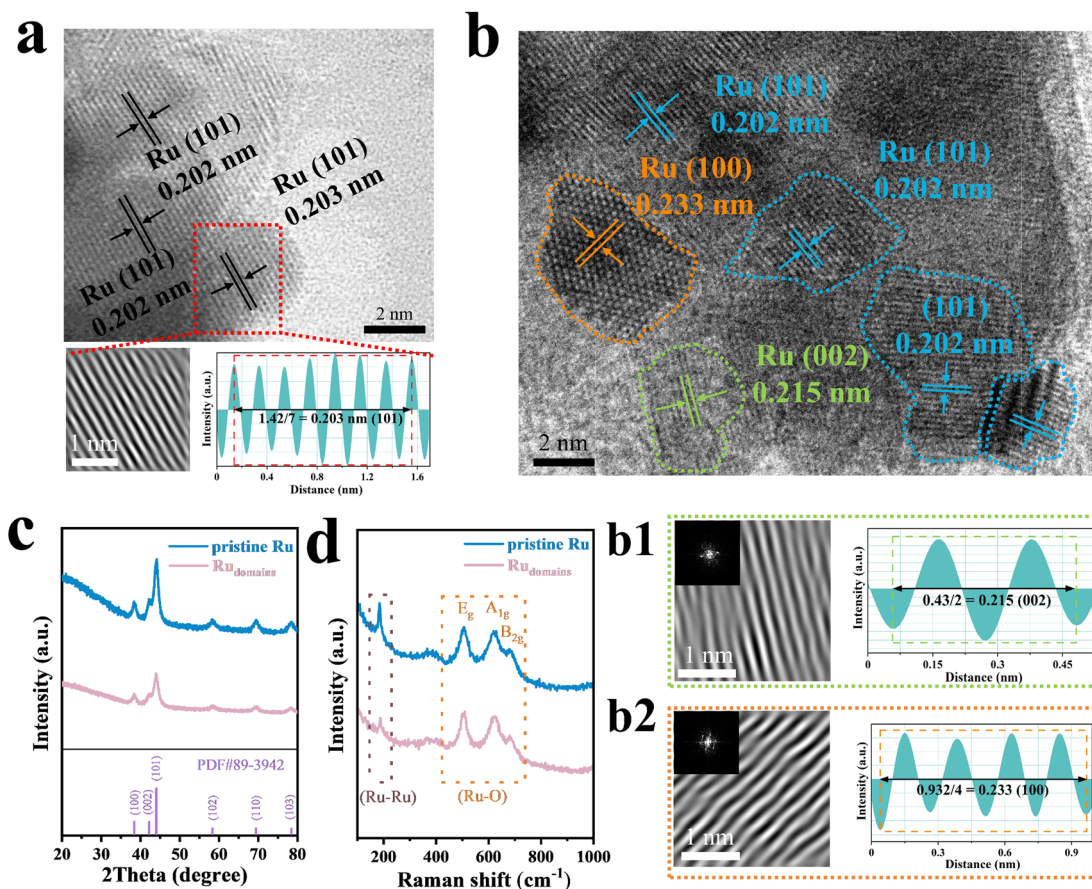


**Fig. 2** (a) HRTEM image of pristine Ru, with IFFT image and the corresponding intensity profiles of the selected area. (b) HRTEM image of Ru<sub>domains</sub>. (b1 and b2) FFT and IFFT images and the corresponding intensity profiles of the selected areas in (b). (c) XRD patterns. (d) Raman spectra.

Fig. S13b† shows the XRD pattern of the relevant sample without nitric acid cleaning. The XRD pattern of unwashed Ru<sub>domains</sub> showed distinct MgO and Mg(OH)<sub>2</sub> phases, but no metallic Mg, indicating that isopropanol has better reducibility towards Ru. Without nitric acid cleaning, the diffraction peaks of Ru<sub>domains</sub> in metallic ruthenium also weakened; therefore, the effect of nitric acid on the ordered crystal structure can be excluded. Additionally, Raman spectra (Fig. 2d and S14†) provided further structural insights. The Raman peak at 189 cm<sup>-1</sup> is associated with the metallic Ru–Ru bond, representing the characteristic vibrational mode of metallic Ru.<sup>37</sup> In contrast to

X-ray photoelectron spectroscopy (XPS) was used to analyze the composition of materials. No Mg signal was detected in all samples, confirming the complete removal of MgO (Fig. S15†).

In contrast, the presence of strong Mg peaks in the unwashed samples (Fig. S16†) highlights the initial structural participation of MgO in the solvothermal growth process, playing a pivotal role in domain formation. For Ru<sub>domains</sub>, the Ru 3p orbital analysis (Fig. 3a and S17a†) reveals a 0.3–0.4 eV positive shift in the Ru 3p<sub>3/2</sub> peak relative to pristine Ru, indicating an electron-deficient environment around Ru atoms. Furthermore, it was deconvoluted to Ru<sup>0</sup> (462.1 eV) and Ru<sup>δ+</sup>

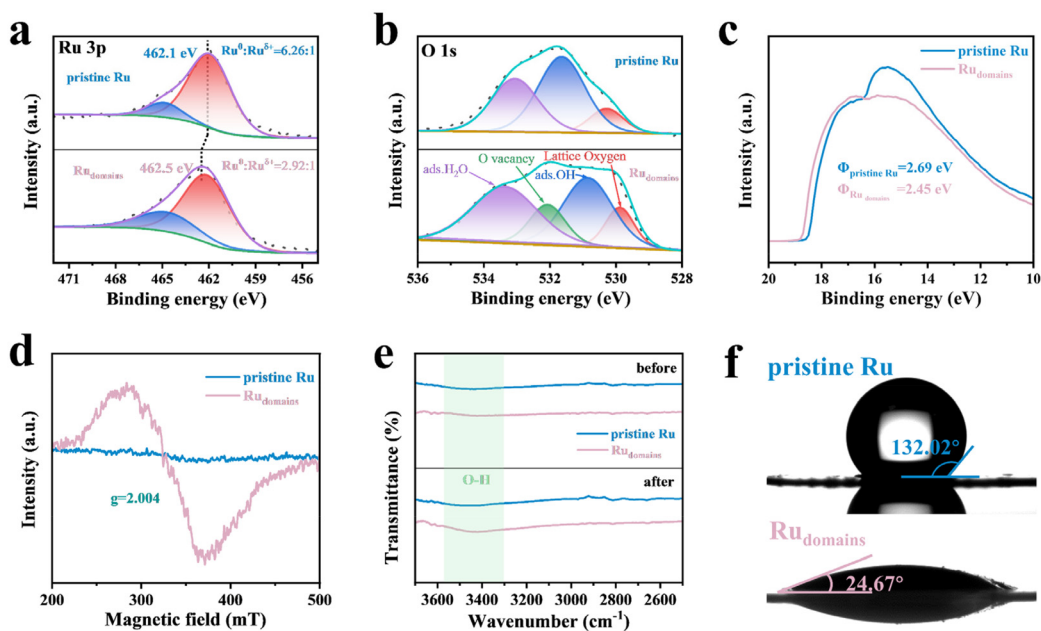


**Fig. 3** Pristine Ru and Ru<sub>domains</sub> (a) XPS spectra of Ru 3p, (b) XPS spectra of O 1s, (c) UPS spectra, (d) EPR spectra, (e) the FTIR profiles before and after the water vapor treatment, and (f) contact angle images.

(465.1 eV), emphasizing the influence of metallic Ru<sup>0</sup> and high-valence Ru<sup>δ+</sup>. The Ru<sup>0</sup>/Ru<sup>δ+</sup> ratio significantly decreases from 6.26 in pristine Ru to 2.92 in Ru<sub>domains</sub>, suggesting increased surface Ru–O interactions, likely arising from abundant interfacial oxygen species at crystal domain boundaries.<sup>40</sup>

Concurrently, the O 1s spectrum (Fig. 3b and S17b†) shows a pronounced increase in both lattice oxygen and oxygen vacancy content in the Ru<sub>domains</sub> sample.<sup>41</sup> These oxygen species are widely recognized to facilitate water dissociation, particularly in the Volmer step of alkaline HER, by enhancing the surface oxophilicity. The coexistence of high-valence Ru<sup>δ+</sup> and oxygen defects suggests a more reactive and hydrophilic surface microenvironment. The crystal domain structure formed during MgO-templated growth both induces preferential (100)/(002) facet exposure and concentrates edge sites with oxygen defects at domain boundaries. This unique configuration facilitates H adsorption, especially during the Volmer step, thereby underpinning the enhanced HER activity.<sup>42</sup> Moreover, inductively coupled plasma (ICP) analysis (Table S1†) confirms the complete removal of Mg after acid etching. The electronic and interfacial properties of the catalysts were further investigated. Fig. 3c shows surface valence band spectra, demonstrating that Ru<sub>domains</sub> exhibits the lowest work function of 2.45 eV. This reduction in the energy barrier for electron emission facilitates more efficient interfacial electron transfer, thereby accelerating proton–electron coupling and enhancing the kinetics of the HER process.<sup>43</sup> The lowered work function is attributed to the increased density of low-coordinated surface atoms and edge states introduced by crystalline domain segmentation. Electron paramagnetic resonance (EPR) spectroscopy is performed at room temperature

(Fig. 3d). A prominent signal at  $g = 2.004$  is observed exclusively in Ru<sub>domains</sub>, attributed to unpaired electrons associated with oxygen vacancies or low-coordination Ru–O species. These paramagnetic centers are predominantly localized at domain boundaries and edge-rich regions—features arising from the MgO-directed domain formation—and act as highly efficient sites for water splitting and electron movement. The water adsorption behavior was further examined by FTIR spectroscopy (Fig. 3e). Upon exposure to water vapor, Ru<sub>domains</sub> displays a significantly intensified O–H stretching band relative to pristine Ru, suggesting that surface Ru–O increases H<sub>2</sub>O affinity.<sup>44</sup> This aligns with the increased density of surface Ru–O species and oxygen vacancies, both indicating a hydrophilic surface nature and facilitating water activation through the Volmer step. This conclusion is supported by water contact angle measurements. The surface of pristine Ru is hydrophobic, with a contact angle measuring 132.02°, whereas Ru<sub>domains</sub> shows a highly hydrophilic interface with a contact angle of only 24.67° (Fig. 3f). This pronounced shift in wettability stems from the formation of oxygenated edge sites and polar terminations at crystalline domain interfaces, which enable more facile access of water molecules to the active regions and ensure continuous hydrogen evolution.<sup>45</sup>

The HER properties of the pristine Ru, Ru<sub>domains</sub>-1, Ru<sub>domains</sub>, Ru<sub>domains</sub>-2 and commercial Pt/C catalysts are compared. Fig. 4a illustrates the linear sweep voltammetry (LSV) curves of the catalysts in 1 M KOH. Ru<sub>domains</sub> delivers the lowest at a density of 10 mA cm<sup>-2</sup>, which is significantly superior to that of pristine Ru (87.4 mV), Ru<sub>domains</sub>-1 (65.5 mV), Ru<sub>domains</sub>-2 (35.5 mV), and commercial Pt/C (40.4 mV), respectively. A similar trend is observed at 20 mA

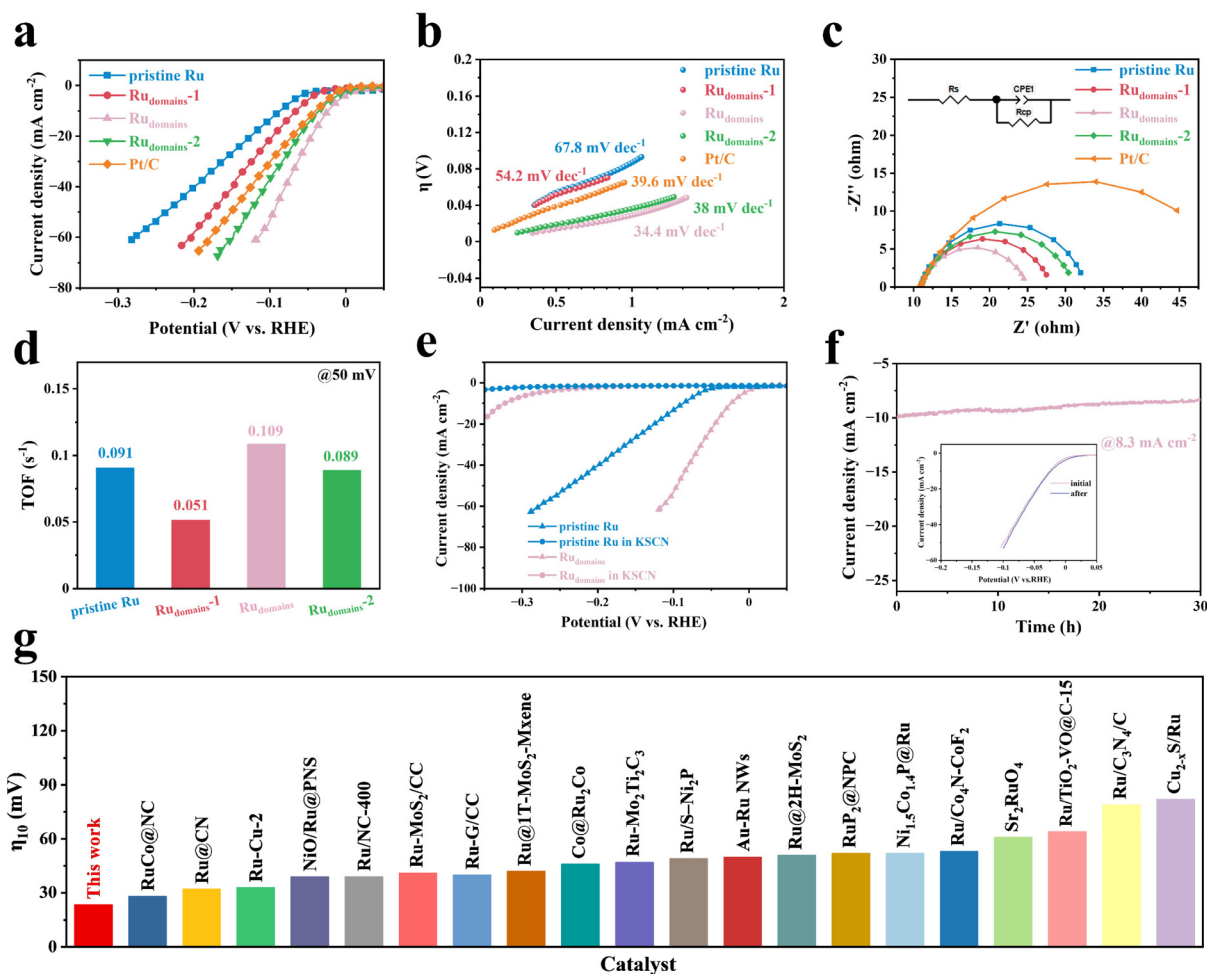


**Fig. 4** HER performance of different catalysts in 1.0 M KOH solution: (a) LSV curves, (b) Tafel plots, (c) EIS spectra, (d) TOFs, (e) LSV curves obtained during HER operation in the KSCN involved electrolyte, (f) chronoamperometric response curves of  $\text{Ru}_{\text{domains}}$  at  $10 \text{ mA cm}^{-2}$ , with LSV polarization curves recorded before and after the chronoamperometry measurement, and (g) comparison of  $\eta_{10}$  for alkaline HER on  $\text{Ru}_{\text{domains}}$  with recently reported Ru-based catalysts; the detailed information on these compared catalysts can be found in the ESI.†

$\text{cm}^{-2}$  (Fig. S18†), abundant domain boundaries and edge sites provide a high density of active centers. The Tafel slope of  $\text{Ru}_{\text{domains}}$  is  $34.4 \text{ mV dec}^{-1}$  (Fig. 4b), much lower than that of pristine Ru ( $67.8 \text{ mV dec}^{-1}$ ),  $\text{Ru}_{\text{domains-1}}$  ( $54.2 \text{ mV dec}^{-1}$ ), and  $\text{Ru}_{\text{domains-2}}$  ( $38 \text{ mV dec}^{-1}$ ), indicating a Volmer–Heyrovsky HER mechanism with accelerated kinetics, where water dissociation is efficiently promoted by edge-enriched Ru–O interfaces, enhancing overall alkaline HER performance.<sup>46</sup> Additionally, electrochemical impedance spectroscopy (EIS, Fig. 4c) further supports the enhanced charge transfer characteristics of  $\text{Ru}_{\text{domains}}$ , which exhibits the lowest charge transfer resistance of  $13 \Omega$  at  $50 \text{ mV}$ . This reduced energy barrier enables more efficient electron flow at the electrode–electrolyte interface, promoting faster reaction kinetics. The intrinsic activity of  $\text{Ru}_{\text{domains}}$  is further verified by its high turnover frequency (TOF) of  $0.109 \text{ H}_2 \text{ s}^{-1}$  at  $50 \text{ mV}$  (Fig. 4d), indicating excellent atomic utilization (CO stripping measurement was used to assess the moles of metal atoms as shown in Fig. S19†).  $\text{SCN}^-$  poisoning experiments (Fig. 4e) demonstrate

that blocking the exposed Ru sites significantly suppresses HER activity, confirming that these Ru centers serve as the principal active sites. In comparison with other advanced Ru-based HER catalysts (Table S2,† and Fig. 4g),  $\text{Ru}_{\text{domains}}$  stands out with its ultralow overpotential and rapid kinetics, highlighting the critical role of nanoscale crystalline domain engineering in promoting edge-rich chemistry and enhancing water dissociation. This is further supported by double-layer capacitance (DLC) measurements (Fig. S20 and S21†), where  $\text{Ru}_{\text{domains}}$  shows the largest electrochemical surface area (ECSA), consistent with its high density of exposed edges and domain boundaries generated *via* the MgO template strategy. Chronoamperometry measurements (Fig. 4f) show that  $\text{Ru}_{\text{domains}}$  retains 83% of its initial current after 30 hours at  $10 \text{ mA cm}^{-2}$ , with minimal deviation between initial and post-reaction polarization curves. The morphology and chemical state of  $\text{Ru}_{\text{domains}}$  remain consistent after a long duration of HER operation, demonstrating excellent electrochemical durability (Fig. S22†). Finally, the pH-universal performance of

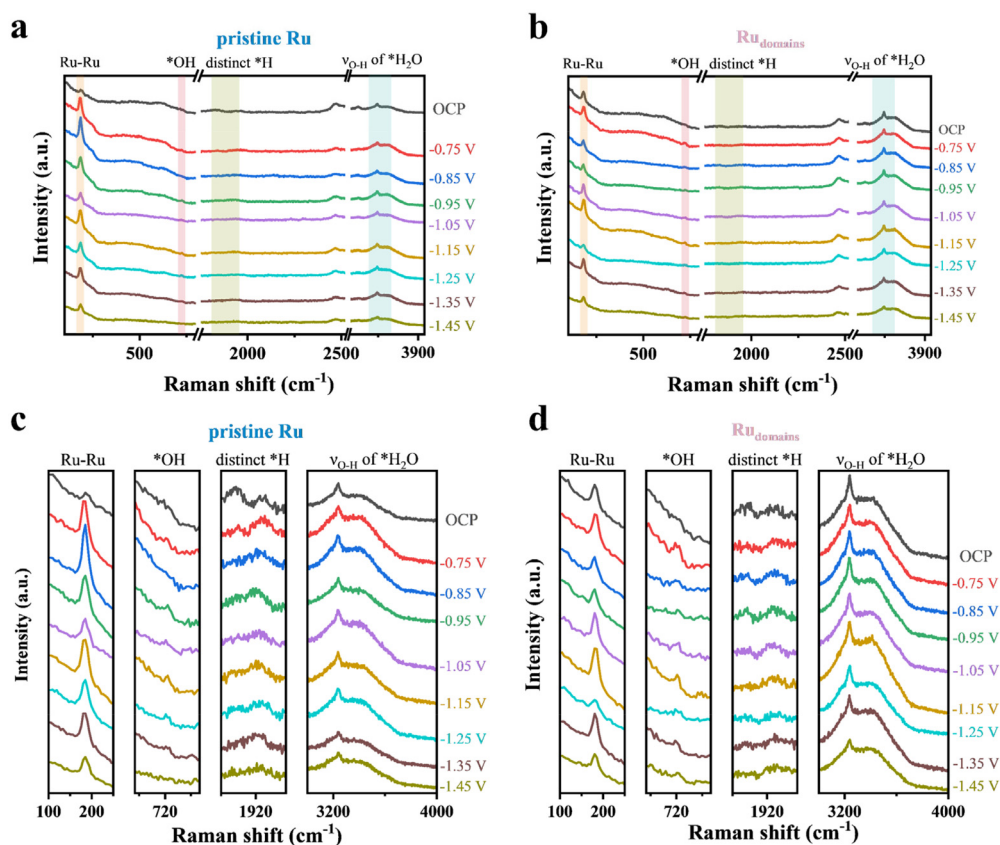


**Fig. 5** *In situ* Raman spectra recorded on (a) pristine Ru and (b)  $\text{Ru}_{\text{domains}}$ . (c) and (d) Magnified spectra of the corresponding vibration regions from (a) and (b), respectively.

$\text{Ru}_{\text{domains}}$  was examined in 0.5 M  $\text{H}_2\text{SO}_4$  and 1.0 M  $\text{Na}_2\text{SO}_4$  electrolytes. As shown in Fig. S23,<sup>†</sup>  $\text{Ru}_{\text{domains}}$  demonstrates superior HER activity across acidic and neutral conditions. This advancement is attributed to the edge-rich crystalline domain design, which both enhances the Ru–H interaction for more rapid  $\text{H}_2$  desorption and improves water adsorption and dissociation, thereby ensuring high activity under diverse operating environments.

For a more detailed examination of the possible catalytic mechanism on a larger scale, *in situ* Raman measurements were conducted on pristine Ru and  $\text{Ru}_{\text{domains}}$  in a 0.1 M KOH solution to track the HER at the surface.

As shown in Fig. 5a and b, both samples initially exhibit characteristic vibrational modes, including Ru–Ru ( $185\text{ cm}^{-1}$ ), adsorbed hydroxyl (\*OH,  $715\text{--}726\text{ cm}^{-1}$ ), and Ru–H stretching bands corresponding to hydrogen adsorbed on metallic Ru ( $1825\text{ cm}^{-1}$ ) and oxidized Ru species ( $1950\text{ cm}^{-1}$ ), as well as interfacial water O–H stretching ( $3420\text{ cm}^{-1}$ ).<sup>47</sup> Compared with pristine Ru (Fig. 5c),  $\text{Ru}_{\text{domains}}$  (Fig. 5d) displays several notable spectral differences that directly reflect its edge-enriched, crystalline domain structure. Firstly, the Ru–H stretching mode at  $\sim 1825\text{ cm}^{-1}$  emerges at lower potentials and increases in intensity more rapidly, suggesting an earlier onset of \*H adsorption and a higher density of metallic  $\text{Ru}^0\text{--H}$  sites.<sup>48</sup> This is consistent with the phenomena observed in

electrochemical measurements, evidencing accelerated Volmer–Heyrovsky HER kinetics. Secondly, the weakened  $\text{Ru}^{\text{II}}\text{--H}$  mode ( $\sim 1950\text{ cm}^{-1}$ ) indicates a more reduced surface environment, likely stabilized by the small crystalline domains and the exposure of low-coordination Ru atoms at edges, which are less susceptible to oxidation under operational potentials. More importantly, the adsorbed \*OH bending ( $\sim 715\text{ cm}^{-1}$ ) and O–H stretching ( $\sim 3420\text{ cm}^{-1}$ ) features show distinct potential-dependent trends for  $\text{Ru}_{\text{domains}}$ , reflecting altered interfacial water structuring and enhanced water dissociation.<sup>49,50</sup> The higher intensity and earlier appearance of these signals for  $\text{Ru}_{\text{domains}}$  imply facilitated water adsorption and faster \*OH generation, confirming more efficient water activation, a critical step in alkaline HER.

## 4. Conclusions

In summary, we present a rational strategy to construct edge-rich Ru catalysts *via* MgO-templated domain engineering. By directing the crystallization of HCP Ru into nanoscale domains with preferential (100) and (002) facet exposure, the resulting  $\text{Ru}_{\text{domains}}$  features abundant low-coordination edge sites and Ru–O motifs enriched with oxygen vacancies, collectively forming an edge-rich chemistry environment.  $\text{Ru}_{\text{domains}}$

achieves an ultralow overpotential of 23.5 mV at 10 mA cm<sup>-2</sup> and a Tafel slope of 34.4 mV dec<sup>-1</sup> in 1 M KOH, outperforming pristine Ru and commercial Pt/C. This performance arises from (1) crystal domain-induced enrichment of low-coordination Ru–O motifs and oxygen vacancies at domain boundaries (these sites exhibit high local charge density and oxophilicity, which synergistically lower the energy barrier for H<sub>2</sub>O adsorption and dissociation, thereby accelerating the Volmer step and improving alkaline HER kinetics) and (2) surface undercoordination induced by crystal plane selective regulation, which adjusts the hydrogen binding free energy ( $\Delta G_{\text{H}^*}$ ) to the optimal range, enhancing the recombination of adsorbed \*H into H<sub>2</sub> through the Heyrovsky step. Overall, this work offers a general and scalable domain-facet engineering approach for activating edge-rich chemistry in Ru-based catalysts, guiding the design of electrocatalysts with high efficiency and broad pH applicability.

## Conflicts of interest

There are no conflicts to declare.

## Data availability

The data supporting this article have been included as part of the ESI.†

## Acknowledgements

The authors acknowledge researcher Qilong Liu for the *in situ* Raman characterization and valuable suggestions.

## References

- 1 Y. Tan, H. Wang, P. Liu, Y. Shen, C. Cheng, A. Hirata, T. Fujita, Z. Tang and M. Chen, Versatile nanoporous bimetallic phosphides towards electrochemical water splitting, *Energy Environ. Sci.*, 2016, **9**, 2257–2261.
- 2 Q. Gong, Y. Wang, Q. Hu, J. Zhou, R. Feng, P. N. Duchesne, P. Zhang, F. Chen, N. Han, Y. Li, C. Jin, Y. Li and S. T. Lee, Ultrasmall and phase-pure W<sub>2</sub>C nanoparticles for efficient electrocatalytic and photoelectrochemical hydrogen evolution, *Nat. Commun.*, 2016, **7**, 13216.
- 3 Q. Ma, H. Jin, F. Xia, H. Xu, J. Zhu, R. Qin, H. Bai, B. Shuai, W. Huang, D. Chen, Z. Li, J. Wu, J. Yu and S. Mu, Ultralow Ru-assisted and vanadium-doped flower-like CoP/Ni<sub>2</sub>P heterostructure for efficient water splitting in alkali and seawater, *J. Mater. Chem. A*, 2021, **9**, 26852–26860.
- 4 Y. Fang, Y. Liu, L. Qi, Y. Xue and Y. Li, 2D graphdiyne: an emerging carbon material, *Chem. Soc. Rev.*, 2022, **51**, 2681–2709.
- 5 X. Kong, C. Zhang, S. Y. Hwang, Q. Chen and Z. Peng, Free-Standing Holey Ni(OH)<sub>2</sub> Nanosheets with Enhanced Activity for Water Oxidation, *Small*, 2017, **13**, 1700334.
- 6 J. Yu, S. Zhao, B. Li and C. Zhu, Interface engineering assisted La<sub>1-x</sub>Sr<sub>x</sub>CoO<sub>3</sub>/FeOOH heterostructure as a high-performance electrocatalyst for oxygen evolution reaction, *Int. J. Hydrogen Energy*, 2024, **80**, 949–955.
- 7 B. Guo, Y. Ding, H. Huo, X. Wen, X. Ren, P. Xu and S. Li, Recent Advances of Transition Metal Basic Salts for Electrocatalytic Oxygen Evolution Reaction and Overall Water Electrolysis, *Nano-Micro Lett.*, 2023, **15**, 57.
- 8 R. T. Liu, Z. L. Xu, F. M. Li, F. Y. Chen, J. Y. Yu, Y. Yan, Y. Chen and B. Y. Xia, Recent advances in proton exchange membrane water electrolysis, *Chem. Soc. Rev.*, 2023, **52**, 5652–5683.
- 9 L. Hui, D. Jia, H. Yu, Y. Xue and Y. Li, Ultrathin Graphdiyne-Wrapped Iron Carbonate Hydroxide Nanosheets toward Efficient Water Splitting, *ACS Appl. Mater. Interfaces*, 2019, **11**, 2618–2625.
- 10 X. Zhang, Y. Dong, Q. Lv, F. Wang, C. Jiang, Y. Wang, J. Dou, Q. Guo, B. Dong and Q. Tang, Boosting hydrogen evolution of nickel phosphide by expanding built-in electric field with tungsten oxide, *Appl. Catal., B*, 2024, **342**, 123440.
- 11 C. Chang, X. Li, S. Wei, Y. Zhao, L. Gong, Y. Zhang, J. Liu and F. Gong, Cross-Scale Process Intensification of Spindle CuO Supported Tungsten Single-Atom Catalysts toward Enhanced Electrochemical Hydrogen Production, *Adv. Energy Mater.*, 2024, **15**, 2402825.
- 12 H. Ling, Q. Yuan, T. Sheng and X. Wang, Dual active site and metal-substrate interface effect endow platinum-ruthenium/molybdenum carbide efficient pH-universal hydrogen evolution reaction, *J. Colloid Interface Sci.*, 2025, **685**, 371–381.
- 13 X. Gao, J. Chen, X. Sun, B. Wu, B. Li, Z. Ning, J. Li and N. Wang, Ru/RuO<sub>2</sub> Nanoparticle Composites with N-Doped Reduced Graphene Oxide as Electrocatalysts for Hydrogen and Oxygen Evolution, *ACS Appl. Nano Mater.*, 2020, **3**, 12269–12277.
- 14 S. Pan, X. Yang, J. Sun, X. Wang, J. Zhu and Y. Fu, Competitive Adsorption Mechanism of Defect-Induced d-Orbital Single Electrons in SrRuO<sub>3</sub> for Alkaline Hydrogen Evolution Reaction, *Adv. Energy Mater.*, 2023, **13**, 2301779.
- 15 C. Hu, L. Zhang and J. Gong, Recent progress made in the mechanism comprehension and design of electrocatalysts for alkaline water splitting, *Energy Environ. Sci.*, 2019, **12**, 2620–2645.
- 16 W. Li, Y. Liu, M. Wu, X. Feng, S. A. T. Redfern, Y. Shang, X. Yong, T. Feng, K. Wu, Z. Liu, B. Li, Z. Chen, J. S. Tse, S. Lu and B. Yang, Carbon-Quantum-Dots-Loaded Ruthenium Nanoparticles as an Efficient Electrocatalyst for Hydrogen Production in Alkaline Media, *Adv. Mater.*, 2018, **30**, 1800676.
- 17 Y. Tong, E. P. Yao, A. Manzi, E. Bladt, K. Wang, M. Doblinger, S. Bals, P. Muller-Buschbaum, A. S. Urban, L. Polavarapu and J. Feldmann, Spontaneous Self-Assembly of Perovskite Nanocrystals into Electronically Coupled

- Supercrystals: Toward Filling the Green Gap, *Adv. Mater.*, 2018, **30**, 1801117.
- 18 Q. He, Y. Zhou, H. Shou, X. Wang, P. Zhang, W. Xu, S. Qiao, C. Wu, H. Liu, D. Liu, S. Chen, R. Long, Z. Qi, X. Wu and L. Song, Synergic Reaction Kinetics over Adjacent Ruthenium Sites for Superb Hydrogen Generation in Alkaline Media, *Adv. Mater.*, 2022, **34**, 2110604.
  - 19 J. Yu, Q. He, G. Yang, W. Zhou, Z. Shao and M. Ni, Recent Advances and Prospective in Ruthenium-Based Materials for Electrochemical Water Splitting, *ACS Catal.*, 2019, **9**, 9973–10011.
  - 20 Y. Chen, Y. Lee, W. Chu and J. Li, Trace Ru-tuned NiO/CNT electrocatalysts outperform benchmark Pt for alkaline hydrogen evolution with superior mass activity, *Chem. Eng. J.*, 2023, **472**, 144922.
  - 21 S. Bolar, S. Shit, N. C. Murmu, P. Samanta and T. Kuila, Activation Strategy of MoS<sub>2</sub> as HER Electrocatalyst through Doping-Induced Lattice Strain, Band Gap Engineering, and Active Crystal Plane Design, *ACS Appl. Mater. Interfaces*, 2021, **13**, 765–780.
  - 22 J. Gu, L. Li, Q. Yang, F. Tian, W. Zhao, Y. Xie, J. Yu, A. Zhang, L. Zhang, H. Li, J. Zhong, J. Jiang, Y. Wang, J. Liu and J. Lu, Twinning Engineering of Platinum/Iridium Nanonets as Turing-Type Catalysts for Efficient Water Splitting, *J. Am. Chem. Soc.*, 2024, **146**, 5355–5365.
  - 23 C. Wang, J. Zhang, K. Miao, M. Long, S. Lai, S. Zhao and X. Kang, Octahedral Nanocrystals of Ru-Doped PtFeNiCuW/CNTs High-Entropy Alloy: High Performance Toward pH-Universal Hydrogen Evolution Reaction, *Adv. Mater.*, 2024, **36**, 2400433.
  - 24 X. Mu, X. Zhang, Z. Chen, Y. Gao, M. Yu, D. Chen, H. Pan, S. Liu, D. Wang and S. Mu, Constructing Symmetry-Mismatched Ru<sub>x</sub>Fe<sub>3-x</sub>O<sub>4</sub> Heterointerface-Supported Ru Clusters for Efficient Hydrogen Evolution and Oxidation Reactions, *Nano Lett.*, 2024, **24**, 1015–1023.
  - 25 G. Ou, F. Wu, K. Huang, N. Hussain, D. Zu, H. Wei, B. Ge, H. Yao, L. Liu, H. Li, Y. Shi and H. Wu, Boosting the Electrocatalytic Water Oxidation Performance of CoFe<sub>2</sub>O<sub>4</sub> Nanoparticles by Surface Defect Engineering, *ACS Appl. Mater. Interfaces*, 2019, **11**, 3978–3983.
  - 26 X. Li, Z. Zhao, X. Meng and Z. Li, Rapid Joule-heating fabrication of Ce-doped Co/CoO on carbon nanotubes for efficiently electrocatalytic hydrogen production, *Appl. Surf. Sci.*, 2024, **669**, 160481.
  - 27 X. Liu, J. Shi, Y. Wu, M. Ma, Y. Wang, Z. Li, X. Cai, Y. Zhang, R. Duan, S. Liu, W. Gao and Z. Liu, Lateral Heterostructures of Defect-Patterned MoS<sub>2</sub> for Efficient Hydrogen Production, *Small*, 2025, **21**, 2411077.
  - 28 S. K. Hyeong, B. J. Moon, A. Lee, M. J. Im, H. Y. Yang, J. H. Choi, S. I. Kim, J. Y. Moon, S. Park, S. K. Jang, T. W. Kim, J. H. Lee, S. Bae and S. K. Lee, Artificial Modulation of the Hydrogen Evolution Reaction Kinetics via Control of Grain Boundaries Density in Mo<sub>2</sub>C Through Laser Processing, *Adv. Funct. Mater.*, 2025, 2422918.
  - 29 C. R. Zhu, D. Gao, J. Ding, D. Chao and J. Wang, TMD-based highly efficient electrocatalysts developed by combined computational and experimental approaches, *Chem. Soc. Rev.*, 2018, **47**, 4332–4356.
  - 30 T. Morishita, T. Tsumura, M. Toyoda, J. Przepiórski, A. W. Morawski, H. Konno and M. Inagaki, A review of the control of pore structure in MgO-templated nanoporous carbons, *Carbon*, 2010, **48**, 2690–2707.
  - 31 R. A. Acedera, A. T. Dumlao, D. D. Matienzo, M. Divinagracia, J. A. Paraggua, P. Y. A. Chuang and J. Ocon, Templated synthesis of transition metal phosphide electrocatalysts for oxygen and hydrogen evolution reactions, *J. Energy Chem.*, 2024, **89**, 646–669.
  - 32 J. Cen, E. Jiang, Y. Zhu, Z. Chen, P. Tsiakaras and P. K. Shen, Enhanced electrocatalytic overall water splitting over novel one-pot synthesized Ru-MoO<sub>3-x</sub> and Fe<sub>3</sub>O<sub>4</sub>-NiFe layered double hydroxide on Ni foam, *Renewable Energy*, 2021, **177**, 1346–1355.
  - 33 J. Zhao, R. Urrego-Ortiz, N. Liao, F. Calle-Vallejo and J. Luo, Rationally designed Ru catalysts supported on TiN for highly efficient and stable hydrogen evolution in alkaline conditions, *Nat. Commun.*, 2024, **15**, 6391.
  - 34 Y. Liu, J. Zhu, L. Yu, Y. Zhao, X. Cao, S. Wei, J. Zeng, H. Chen, Z. Lu, B. Chen, G. Zhang, L. Zhong and Y. Qiu, Electrically driven phosphorus dissolution from iron-nickel phosphate surfaces exposing highly active sites for oxygen evolution reaction, *J. Colloid Interface Sci.*, 2025, **683**, 197–206.
  - 35 Y. Wang, Y. Qin, R. Wen, L. Wang, M. Dou and F. Wang, High-Performance Low-Iridium Catalyst for Water Oxidation: Breaking Long-Ranged Order of IrO<sub>2</sub> by Neodymium Doping, *Small*, 2024, **20**, 2401964.
  - 36 D. Prieur, W. Bonani, K. Popa, O. Walter, K. W. Kriegsman, M. H. Engelhard, X. Guo, R. Eloiardi, T. Gouder, A. Beck, T. Vitova, A. C. Scheinost, K. Kvashnina and P. Martin, Size Dependence of Lattice Parameter and Electronic Structure in CeO<sub>2</sub> Nanoparticles, *Inorg. Chem.*, 2020, **59**, 5760–5767.
  - 37 J. Xu and X. Kong, Amorphous/Crystalline Heterophase Ruthenium Nanosheets for pH-Universal Hydrogen Evolution, *Small Methods*, 2022, **6**, 2101432.
  - 38 S. Y. Mar, C. S. Chen, Y. S. Huang and K. K. Tiong, Characterization of RuO<sub>2</sub> thin films by Raman spectroscopy, *Appl. Surf. Sci.*, 1995, **90**, 497–504.
  - 39 S. Zuo, Z. P. Wu, D. Xu, R. Ahmad, L. Zheng, J. Zhang, L. Zhao, W. Huang, H. Al Qahtani, Y. Han, L. Cavallo and H. Zhang, Local compressive strain-induced anti-corrosion over isolated Ru-decorated Co<sub>3</sub>O<sub>4</sub> for efficient acidic oxygen evolution, *Nat. Commun.*, 2024, **15**, 9514.
  - 40 S. Zhu, Z. Li, L. Hou, M. G. Kim, H. Jang, S. Liu and X. Liu, Revealing The Role of Electronic Asymmetry on Supported Ru Nanoclusters for Alkaline Hydrogen Evolution Reaction, *Adv. Funct. Mater.*, 2023, **34**, 2314899.
  - 41 J. Jin, X. Han, Y. Fang, Z. Zhang, Y. Li, T. Zhang, A. Han and J. Liu, Microenvironment Engineering of Ru Single-Atom Catalysts by Regulating the Cation Vacancies in NiFe-Layered Double Hydroxides, *Adv. Funct. Mater.*, 2021, **32**, 2109218.

- 42 X. Kong, J. Xu, Z. Ju and C. Chen, Durable Ru Nanocrystal with HfO<sub>2</sub> Modification for Acidic Overall Water Splitting, *Nano-Micro Lett.*, 2024, **16**, 185.
- 43 X. Chen, L. Ye, W. Wu, S. Chen, Z. Wang, Y. Zhu, H. Jiang, R. Chen and N. Cheng, Compressed Ru skin on atomic-ordered hexagonal Ru-Ni enabling rapid Volmer-Tafel kinetics for efficient alkaline hydrogen evolution, *Chem. Eng. J.*, 2024, **487**, 150457.
- 44 Q. Hu, J. Cao, S. Qi, N. Meng, J. Zhao, T. Huang, J. You, T. Liang, C. Shang, J. Yu, H. Yang and C. He, Constructing Unsaturated Ru Atom Arrays Confined in Mn Oxides to Boost Neutral Water Reduction, *Angew. Chem., Int. Ed.*, 2025, **64**, e202416402.
- 45 X. Zhong, S. Xie and Z. Guo, The Challenge of Superhydrophobicity: Environmentally Facilitated Cassie-Wenzel Transitions and Structural Design, *Adv. Sci.*, 2024, **11**, 2305961.
- 46 J. Ding, Q. Shao, Y. Feng and X. Huang, Ruthenium-nickel sandwiched nanoplates for efficient water splitting electrocatalysis, *Nano Energy*, 2018, **47**, 1–7.
- 47 X. Chen, X. T. Wang, J. B. Le, S. M. Li, X. Wang, Y. J. Zhang, P. Radjenovic, Y. Zhao, Y. H. Wang, X. M. Lin, J. C. Dong and J. F. Li, Revealing the role of interfacial water and key intermediates at ruthenium surfaces in the alkaline hydrogen evolution reaction, *Nat. Commun.*, 2023, **14**, 5289.
- 48 S. Zhu, X. Qin, F. Xiao, S. Yang, Y. Xu, Z. Tan, J. Li, J. Yan, Q. Chen, M. Chen and M. Shao, The role of ruthenium in improving the kinetics of hydrogen oxidation and evolution reactions of platinum, *Nat. Catal.*, 2021, **4**, 711–718.
- 49 S. Zhu, X. Qin, Y. Yao and M. Shao, pH-Dependent Hydrogen and Water Binding Energies on Platinum Surfaces as Directly Probed through Surface-Enhanced Infrared Absorption Spectroscopy, *J. Am. Chem. Soc.*, 2020, **142**, 8748–8754.
- 50 Z. Zhao, J. Sun, X. Li, S. Qin, C. Li, Z. Zhang, Z. Li and X. Meng, Engineering active and robust alloy-based electrocatalyst by rapid Joule-heating toward ampere-level hydrogen evolution, *Nat. Commun.*, 2024, **15**, 7475.